Single-Cell Spatial Proteomics Analyses of Head and Neck Squamous Cell Carcinoma Reveal Tumor Heterogeneity and Immune Architectures Associated with Clinical Outcome

Katie E. Blise[a], Shamilene Sivagnanam[b], Grace L. Banik[c,*], Lisa M. Coussens[d], and Jeremy Goecks[a,**]

[a]Department of Biomedical Engineering, Oregon Health & Science University, Portland, OR USA
[b]Program in Computational Biology, Department of Cell, Developmental & Cancer Biology, Oregon Health & Science University, Portland, OR USA
[c]Departments of Cell, Developmental & Cancer Biology, Otolaryngology-Head & Neck Surgery, Oregon Health & Science University, Portland, OR USA
[d]Department of Cell, Developmental & Cancer Biology, and Knight Cancer Institute, Oregon Health & Science University, Portland, OR USA
*Current affiliation: Division of Otolaryngology, Children's Hospital of Philadelphia, Philadelphia, PA USA
**Corresponding author

Correspondence:
Jeremy Goecks, Ph.D.
Associate Professor, Department of Biomedical Engineering
Oregon Health & Science University
3181 SW Sam Jackson Park Road, Mail Code: KR-COM, Portland, OR 97239
Tel: 503-494-0490, Email: goecksj@ohsu.edu

Running Title: Single-cell spatial analysis of head and neck cancer

Keywords: head and neck squamous cell carcinoma, spatial proteomics, tumor microenvironment, immune compartmentalization, tumor heterogeneity

Funding: LMC acknowledges funding from the National Cancer Institute (NCI) of the National Institutes of Health under award numbers U01CA224012, R01CA223150, R01CA226909, and R21HD099367 and funding from the Brenden-Colson Center for Pancreatic Care at Oregon Health & Science University (OHSU). JG acknowledges funding under award number U24CA231877. LMC and JG acknowledge funding from the OHSU Knight Cancer Institute, NCI award number U2CCA233280, and the Prospect Creek Foundation to the OHSU SMMART (Serial Measurement of Molecular and Architectural Responses to Therapy) Program. The content is solely the responsibility of the authors and does not necessarily represent the official views of the National Institutes of Health, OHSU, or the Knight Cancer Institute.

Conflict of Interests: L.M. Coussens is a paid consultant for Cell Signaling Technologies, AbbVie Inc., and Shasqi Inc., received reagent and/or research support from Plexxikon Inc., Pharmacyclics, Inc., Acerta Pharma, LLC, Deciphera Pharmaceuticals, LLC, Genentech, Inc., Roche Glycart AG, Syndax Pharmaceuticals Inc., Innate Pharma, NanoString Technologies, and Cell Signaling Technologies, is a member of the Scientific Advisory Boards of Syndax Pharmaceuticals, Carisma Therapeutics, Zymeworks, Inc, Verseau Therapeutics, Cytomix Therapeutics, Inc., and Kineta Inc, and is a member of the Lustgarten Therapeutics Advisory working group. No potential conflicts of interest were disclosed by the other authors.

Word count, abstract: 160
Word count, text: 4216
Figure count: 4
Table count: 2

ABSTRACT

Recent research has provided compelling evidence that the spatial organization of cells within the tumor-immune microenvironment (TiME) of solid tumors correlates with survival and response to therapy in numerous cancer types. Here, we report results of a quantitative single-cell spatial analysis of the TiME of primary and recurrent human head and neck squamous cell carcinoma (HNSCC) tumors, that builds upon our initial longitudinal study of these same HNSCCs that annotated immune complexity at near single cell resolution. Herein, we extended multiple spatial algorithms to quantify spatial landscapes of immune cells within TiMEs. Most notably, we report that spatial compartmentalization, rather than mixing, between neoplastic tumor cells and immune cells is associated with longer patient survival, as well as revealing mesenchymal spatial cellular neighborhoods and their association with improved patient outcomes. Results reported herein are concordant with studies in other tumor types, thus indicating that cellular heterogeneity within tumors trends with spatial TiME features, and are likely prognostic for patient survival.

INTRODUCTION

Tumor microenvironments, comprising both neoplastic tumor cells and recruited stromal cells of various lineages, including a diverse assemblage of immune, mesenchymal, and vascular cells, play a key role in both de novo progression of tumors and regulating response to therapies (1-3). Numerous studies have reported that the spatial organization of the tumor-immune microenvironment (TiME), beyond just the types and quantities of cells present in the TiME, is prognostic for survival and response to therapy in multiple cancer types (4-13). Measures that quantify this spatial organization can range from simple density ratios within specific tumor regions (14), such as the Immunoscore (15), a now commonly used biomarker for tumor staging, to more complex measures that account for the precise locations of specific cells relative to other cells, such as mixing scores(4) and cellular neighborhood measures (7). These more advanced spatial quantifications are a result of emerging single-cell multiplex tissue imaging modalities (4, 6, 7, 16-18), that provide detailed phenotypic and effector statuses for each cell, while maintaining the spatial context of the tissue assayed. Knowing the precise locations of cells in the TiME enables a deeper understanding of how cells interact within the tumor, as both direct and indirect cell signaling mechanisms require cells to be near, if not directly adjacent to one another (19). This understanding can then aid treatment decisions, as many therapies require spatial proximity of specific cell types for efficacy (10). Given that single-cell imaging technologies are still quite new, there is much to be discovered regarding how the spatial organization of cells within the TiME relates to clinical outcome, and may be used for patient stratification decisions for therapy.

We previously developed a multiplex immunohistochemistry (mIHC) imaging platform to aid studies investigating the immune contexture of solid tumors and their response to therapies, at the single-cell level (16, 17). Using a sequential antibody staining protocol, detection of 25-50 proteins can be enumerated at single-cell resolution across a single

formalin-fixed paraffin-embedded (FFPE) tissue section. This enables single-cell phenotyping of discrete leukocyte lineages, capturing their phenotypic effector statuses, and importantly, reveals their spatial relationships to other cells in the tissue section. Utilizing this mIHC approach on a small cohort of primary and recurrent human head and neck squamous cell carcinomas (HNSCCs), we found immune contextures associated with disease recurrence, most notable that macrophage to $CD8^+$ T cell ratios within tumor tissues correlate with outcomes (16, 17). HNSCC is the sixth leading form of cancer worldwide (20), and it accounts for more than 10,000 deaths per year in the US alone (21). While patients harboring human papilloma virus (HPV) within neoplastic cells tend to exhibit a better prognosis, their HPV-negative [HPV(-)] counterparts typically exhibit T cell suppressive TiMEs and have a significantly greater risk of recurrence and shorter 3-year survival (22-24). There is a critical need to improve the understanding of HNSCC TiMEs to enable better patient stratification for therapy, as well as identify new targets that could be leveraged for therapeutic intervention to improve outcome, particularly for patients with HPV(-) tumors who currently lack promising therapeutic options.

Here, we built upon our initial study that annotated FFPE sections of nine HPV(-) matched primary newly diagnosed versus their recurrent HNSCCs via our mIHC proteomics imaging platform for TiME leukocyte lineage contexture (17). We measured tumor heterogeneity and compositional changes from primary to recurrent tumors and, importantly, deployed multiple spatial algorithms to quantify the spatial organization of the TiMEs. Finally, we correlated these spatial features with survival and identified TiME architectures associated with survival that could be used to stratify future patients for therapy. Overall, our results are concordant with those from other studies, indicating that the features identified herein are likely shared and prognostic across cancer types.

METHODS

Multiplex immunohistochemistry data generation

mIHC is an immunohistochemical-based imaging platform that evaluates sequentially stained immune lineage epitope-specific antibodies for immunodetection on FFPE tissue sections (16, 17). Using our computational image processing workflow along with a hierarchical gating strategy, we are able to phenotype single cells while maintaining the Cartesian coordinates of each cell on the tissue section. We applied the mIHC pipeline to analyze matched primary and recurrent FFPE tissue specimens from nine HPV(-) HNSCC patients. We sequentially stained for 29 antibodies and gated cells as neoplastic tumor, stromal (mesenchymal), or one of seven different leukocyte subtypes spanning both lymphoid and myeloid lineages (**Table 1**). One to three regions of 2500^2 μm^2 each were assayed with mIHC per tumor resection. Patient characteristics and parameters of patient consent are as reported in Banik et al (17). Briefly, study subjects included nine patients with recurrent HNSCC after definitive surgery, chemotherapy, and/or radiation therapy. Matched FFPE tissue specimens from the newly diagnosed primary and recurrent primary tumors for each patient were obtained from the Oregon Health and Science University Knight Biolibrary. Tissue specimens were deidentified

and coded with a unique identifier prior to analysis. Demographic and clinical data including HPV status, tobacco and alcohol use, treatment regimens, and survival outcomes was collected. All HNSCC tumors were staged according to the 8th edition AJCC/UIC TNM classification and cohort characteristics are shown in **Table 2** (17). All studies involving human tissue were approved by institutional IRB (protocol #809 and #3609), and written informed consent was obtained.

Tumor heterogeneity analyses

The Kullback-Leibler divergence was calculated using the entropy function from the Scipy Python package (25). The distribution of each individual tumor region's cellular composition was compared to the tumor's average cellular composition distribution. Log base 2 was used for the calculation. Unsupervised hierarchical clustering of each tumor region was performed using the normalized percent contribution of each cell type present as the features. Euclidean distance was used to determine distances between observations.

Mixing score analysis

Keren et al. developed a mixing score to quantify the ratio of neoplastic and immune cell spatial interactions (4). This score is defined as the number of interactions between neoplastic tumor cells and immune cells divided by the number of interactions between immune cells and another immune cell within a tumor region. We defined there to be an interaction between two cells if their centers [the (x,y) coordinates provided by mIHC] were within 15 μm from one another. We used the median mixing score value (0.1034) for all primary tumors as the threshold to distinguish between mixed and compartmentalized spatial organization groups. Tumor regions with a mixing score of greater than 0.1034 were defined as mixed. Tumor regions with a mixing score of less than 0.1034 were defined as compartmentalized. We used a density threshold of less than 250 immune cells per 800^2 μm^2 to define tumor regions as cold. We chose this threshold to match that used by Keren et al.

Cellular neighborhood clustering analyses

Cellular neighborhoods were defined by drawing a circle of a specified radius around all seed cells of a given phenotype. Cells whose centers were inside the circle were considered neighbors of that seed cell and contributed to that cell's neighborhood. All neighborhoods across all tumor regions were then clustered using scikit-learn's MiniBatchKMeans function (26) to perform K-means clustering according to their normalized cellular composition. The elbow method was used to determine the number of clusters to form. Each resulting cluster was comprised of neighborhoods with a similar cellular makeup.

Statistics

Independent t-tests were used to determine statistically significant differences for independent samples whose differences followed a normal distribution. Mann-Whitney U tests were used to determine statistically significant differences for independent samples whose differences did not follow a normal distribution. Paired t-tests were used to determine statistically significant differences for paired samples whose differences followed a normal distribution. Wilcoxon signed rank tests were used to determine statistically significant differences for paired samples whose differences did not follow a normal distribution. P-values less than 0.05 were considered statistically significant. All statistical calculations were performed with the Scipy package using Python software (25).

Survival analyses

Kaplan-Meier curves were generated and a log-rank test was performed using the lifelines package with Python software (27). P-values less than 0.05 were considered statistically significant.

Data and software availability

All of the data produced by our mIHC computational image processing pipeline, including protein abundance, cell phenotype, and cell location information saved in the form of a matrix, in addition to survival data, is available for download at Zenodo (https://doi.org/10.5281/zenodo.4584441). All computational analyses in this study were performed using Python software, version 3.6.5. The code created to produce the results of this study is available at https://github.com/kblise/HNSCC_mIHC_paper.

RESULTS

Immune contexture of HNSCC

All mIHC data for this study was generated using the protocol described in Banik et al (17). Single cells were phenotyped in 47 tumor regions from nine primary and nine matched recurrent tumors according to the gating strategy shown in **Table 1**, and their locations within the tumor region were reported as Cartesian coordinates. Patient demographic and clinical data is shown in **Table 2** (17). With this data, we investigated tumor heterogeneity both within and across patient samples, quantified the spatial architecture of the TiME using a mixing score and a neighborhood clustering method, associated spatial architectures with clinical outcome, and performed additional analyses to explain these prognostic features.

Single-cell analyses reveal varying degrees of tumor heterogeneity

To address the question of how cellular composition varies across tumor regions, we assessed tumor heterogeneity at multiple levels, including intra-tumoral, inter-tumoral, and inter-patient cellular heterogeneity by calculating the Kullback-Leibler (KL) divergence for each region, performing hierarchical clustering, and conducting a

242 principal component analysis (PCA). The fraction of each cell type present per region
243 was first computed across all eighteen tumors (**Figure 1A,B**). Within individual tumors,
244 there was less variability in the number of immune cells present across regions as
245 compared to the number of neoplastic and non-immune cells present. Our interpretation
246 of this finding was that the neoplastic cells and non-immune cell populations are
247 generally the main drivers of intra-tumoral heterogeneity. To further assess this intra-
248 tumoral heterogeneity in a more quantitative way, we calculated the KL divergence of
249 each region's distribution of cell types present, as compared to its tumor's average cell
250 type distribution. KL divergence is a measure of how similar two distributions are; this
251 approach has been used previously to quantify tumor heterogeneity (6). We found that
252 all regions had minimal KL divergence values (KL < 0.35; **Figure 1C**), signifying a low
253 degree of intra-tumoral heterogeneity.
254
255 To investigate inter-tumoral heterogeneity, we performed unsupervised hierarchical
256 clustering on the 47 tumor regions based on their normalized cellular composition
257 (**Figure 1D**). We found that only one patient (in green at the bottom of the heatmap)
258 contained all five tumor regions clustering together, independent of primary or recurrent
259 state. All other patients' tumors exhibited a greater degree of inter-tumoral
260 heterogeneity, as demonstrated by the distance between primary and recurrent tumor
261 regions in the heatmap's accompanying dendrogram (**Figure 1D**). Finally, we assessed
262 inter-patient tumor heterogeneity, and found that regions evaluated from the same
263 patient tended to cluster together more than regions evaluated from different patients
264 (**Figure 1D**), indicating increased tumor heterogeneity between patients as compared to
265 between samples from the same patient. PCA results also supported these
266 observations (**Figure 1E**).
267
268 **TiME cellular composition altered by therapy**
269
270 Multiple studies have reported differences in TiME cellular makeup (28, 29) and tumor
271 clonal diversity (30) between primary and recurrent tumors. To detect whether any
272 immune contexture changes existed following therapy in our cohort, we analyzed the
273 cellular composition of primary tumors as compared to their recurrent tumors. All
274 patients received combination therapy of cisplatin or cetuximab accompanied by
275 radiation following surgical resections of their primary tumors. We used the average
276 fraction of each cell type present across regions for a given tumor and compared
277 primary tumor composition to their matched recurrent tumor composition. We observed
278 a significant difference in the fraction of B cells present in recurrent tumors following
279 therapy for all patients (p=0.004, **Figure 2A**), with no other common differences found
280 across patients for any other immune cell type (**Figure 2B**). Further, hierarchical
281 clustering and PCA results did not yield discrete clusters of regions grouped by their
282 tumor status (primary or recurrent) (**Figure 1D, 2C**). We then questioned whether
283 subsets of patients contained similar compositional changes to their TiMEs. To address
284 this question, we performed unsupervised hierarchical clustering on the normalized
285 average change in cellular composition across all cell types. This resulted in two distinct
286 groups of patients; these appear to be most different from one another in the relative
287 degree of change in their $CD8^+$ T cell, $CD4^+$ T helper, and dendritic cell populations

(**Figure 2D**). Interestingly, the two patients that received cetuximab (orange and purple), rather than cisplatin, clustered together within one of these groups and had similar overall changes to their tumor compositions following therapy. Together, these results indicate that there were shared trends in TiME composition changes for subsets of patients specific to therapy, and regardless of therapy, all patients saw a significant decrease in B cells from primary to recurrent tumors.

TiME cellular composition associated with survival

Prior research has revealed that increased $CD8^+$ T cell abundance is associated with better outcomes in HNSCC (31-34). Using the average fraction of $CD8^+$ T cells present in primary tumors, no significant association with survival was found (p=0.423, **Figure 2E**). However, patients with a smaller fraction of macrophages present in their primary tumors had better progression free survival (PFS) (p=0.017, **Figure 2F**). These findings are supported by other studies that also identified higher levels of macrophages associated with more aggressive tumors and decreased survival (35, 36). These findings expand on the results of our prior study, which reported that patients with myeloid-inflamed tumors demonstrated decreased PFS than those with lymphoid inflamed tumors (17). Here we report that this difference can be attributed to a single tumor feature—the fraction of macrophages present. We also found that patients with a greater fraction of other non-immune cells ($PANCK^-$, $CD45^-$) correlated with improved PFS (p=0.003, **Figure 2G**), with no other cell types evaluated demonstrating an association with survival.

Quantifying the spatial organization of tumor and immune cells

To investigate if TiME cellular spatial relationships were prognostic in our cohort of primary and recurrent HNSCC as has been reported in other cancer types (5-13), we deployed a mixing score, which was used previously to analyze immune cell spatial compartmentalization in triple negative breast cancers (4). To do this, we quantified the number of immune and neoplastic tumor cells within 15 μm of each other, then divided by the number of immune cells within 15 μm from another immune cell. We labeled each region as mixed or compartmentalized using the median mixing score value for all primary tumors as the threshold (**Figure 3A,B**; see Methods). This threshold categorized tumor regions as mixed when at least one neoplastic tumor cell was within 15 μm from an immune cell for approximately every ten immune cells within 15 μm from another immune cell. Tumor regions were compartmentalized when this ratio was smaller. Regions with fewer than 250 $CD45^+$ immune cells per 800^2 μm^2 present were labeled as cold. Of the 47 total tumor regions, 23 were mixed, 20 were compartmentalized, and four were cold.

After calculating the mixing score for each region, we explored how cellular composition related to spatial organization. Regions with more mixing between neoplastic cells and immune cells often demonstrated higher presence of neoplastic cells than those with higher compartmentalization (**Figure 3C**). This is unsurprising given the equation for the mixing score, as more neoplastic cells will inevitably only contribute to the numerator of

the score, and thus will increase the overall score. However, regions with more compartmentalization between neoplastic cells and immune cells often also contained increased counts of alpha smooth muscle actin (αSMA)$^+$ mesenchymal cells as compared to those with higher mixing (**Figure 3D**). This result was intriguing because these cells have no effect on the mixing score, yet there is a clear association between composition and organization. This association is further demonstrated by PCA, where regions of similar cellular composition cluster together and also tend to contain similar spatial organizations (**Figure 3E**).

We next examined associations between biomarker expression reflecting on bioeffector phenotypes of leukocytes and mixing scores for each tumor region. Mixed regions contained a greater proportion of neoplastic cells expressing immunoregulatory proteins, such as PD-1 and PD-L1, than compartmentalized regions (p=0.0003, p=0.015, **Figure 3F**). We also found that compartmentalized regions contained a greater proportion of lymphocytes (CD8$^+$ T cells, CD4$^+$ T cells, and B cells) expressing the proliferation marker Ki-67 (p=0.020, **Figure 3G**).

Spatial compartmentalization associated with longer survival

To investigate how spatial mixing correlated with PFS or patient outcome, we averaged the mixing score across regions and assigned a final mixing score and spatial label for each tumor. Patients with more compartmentalization between neoplastic cells and immune cells in their primary tumors exhibited longer PFS than those with more mixing between these cell types (p=0.027, **Figure 3H**).

In addition to quantifying TiME spatial organization using a mixing score, we also computed cellular neighborhoods, that were then clustered to identify common spatial features across tumors. Neighborhoods represent physical groupings of cells within a set distance threshold from a seed cell (**Figure 4A**). Each cell within the distance threshold was deemed a neighbor of the seed cell, contributing to that seed cell's neighborhood's composition. After identifying all neighborhoods for each seed cell present across all tumor regions, neighborhoods were grouped with K-means clustering, using the fraction of each cell type present in the neighborhoods as the clustering features. This revealed clusters of neighborhoods with similar cellular makeups. We then used the average neighbor composition of each cluster to perform survival analyses.

Given the relationship between mixing score and αSMA$^+$ mesenchymal cell abundance, we applied our neighborhood clustering analysis with αSMA$^+$ cells as the seed cells. We used a distance threshold of 22.5 μm, as this produced neighborhoods with an average of approximately ten neighbors present. A recent study involving cellular neighborhood analyses employed a method that selected the ten nearest spatial neighbors of the seed cell, regardless of the distance between the seed cell and its neighbors (7). By setting a distance threshold of 22.5 μm, our method required the cells be close, if not directly touching, while still capturing enough neighbors to cluster on. Clustering results yielded six groups, each different in their composition (**Figure 4B**). αSMA$^+$ cell neighborhoods

380 in cluster 1 contained a majority of αSMA$^+$ cells as the neighbors. Cluster 2 contained
381 both αSMA$^+$ cells as well as other non-immune (CD45$^-$), non-neoplastic cells (panCK$^-$)
382 as neighbors. Cluster 3 was defined by its large proportion of panCK$^+$ neoplastic cells,
383 whereas Cluster 4 consisted of roughly half CD45$^+$ immune cells and half other non-
384 immune, non-neoplastic cells. Cluster 5 contained the highest proportion of CD45$^+$
385 immune cells, and cluster 6 was dominated by other non-immune and non-neoplastic
386 cells.
387
388 We found that patients with a greater proportion of their αSMA$^+$ cells in clusters 2 and 6
389 in their primary tumors demonstrated longer PFS (cluster 2: p=0.059, cluster 6:
390 p=0.003, **Figure 4C,D**), thus indicating that patients whose αSMA$^+$ cells were
391 predominantly surrounded by αSMA$^+$ cells or other non-immune, non-neoplastic cells in
392 their TiMEs were associated with better outcome. In addition, patients with a greater
393 proportion of their αSMA$^+$ cells belonging to cluster 3, which included a large number of
394 neoplastic cells, in their primary tumors demonstrated shorter PFS (p=0.047, **Figure**
395 **4E**).
396

397 # DISCUSSION

398
399 The significant role that TiME cellular composition plays in tumor progression and
400 response to therapy has been accepted for over a decade (37). However, recent
401 findings powered by single-cell proteomics imaging technologies have found that the
402 spatial organization of the cells present in the TiME also plays a critical role (4-13). It is
403 still unclear exactly which spatial features are important in dictating response to therapy
404 or clinical outcome, as well as whether these features are shared across cancer types,
405 and how they could be leveraged for therapeutic decisions and patient stratification.
406 Here, we leveraged single-cell spatial proteomics data generated by our mIHC
407 immunoassay-based imaging platform to quantitatively assess the TiME of nine
408 matched primary and recurrent HPV(-) HNSCCs in order to identify possible prognostic
409 spatial features. Our results provide novel insights into the heterogeneity and spatial
410 landscape of HPV(-) HNSCCs, and highlight possible TiME spatial layouts that may
411 impact clinical outcome across cancer types.
412
413 Despite the fact that HPV(-) HNSCCs often contain limited immune infiltrates (22), our
414 analyses revealed significant differences in the immune cell spatial organization within
415 these tumors that were associated with survival, highlighting the importance of
416 considering the spatial context of the TiME. Most strikingly, patients whose primary
417 tumors contained more compartmentalization between their tumor cell and immune cell
418 populations demonstrated longer PFS. This correlation was also identified in a similar
419 analysis of triple negative breast cancer patients (4), indicating that a
420 compartmentalized spatial architecture may play a favorable role in survival across
421 cancer types. Our analyses of functional marker expression indicate that the immune
422 cells in regions of compartmentalization are proliferating and are perhaps subject to
423 reduced direct regulation by neoplastic tumor cells (38-42) than those in regions of
424 mixing. This increased proliferation and decreased regulation of immune cells in
425 compartmentalized tumors may contribute to improved survival. We also found that the

presence of spatial cellular neighborhoods consisting of αSMA$^+$ cells and other non-immune and non-neoplastic cells surrounding αSMA$^+$ cells was associated with longer survival. On the contrary, the presence of cellular neighborhoods consisting of neoplastic tumor cells surrounding αSMA$^+$ cells was associated with shorter survival. Given that αSMA is a common marker for cancer-associated fibroblasts (20, 43), whose presence in tumors tends to be associated with tumor growth, metastasis, and resistance to therapy (44-47), our results indicate that beyond just the abundance of these cells, their spatial organization may play a crucial role in determining how a tumor progresses, and/or how it responds to standard therapy. Our cellular neighborhood analyses highlight the importance of considering how multiple cells can work in tandem with one another, beyond single cell-cell interactions, to impact TiME organization, and ultimately, clinical outcome.

We also found concordance between the results from our heterogeneity and composition analyses and those from several other studies. Our results are similar to a study that clustered HNSCC biopsies based on their neoplastic and immune gene signatures as determined by RNA-sequencing, and reported that samples from the same patient were more similar to each other than samples from different patients (48). This trend has also been observed across cancer types, including melanoma (49), hepatocellular carcinoma (50), pancreatic ductal adenocarcinoma (51), and breast cancer (52). Finally, we found that decreased macrophage abundance was associated with longer survival, which has previously been reported in head and neck cancers (35, 36). Collectively, these results demonstrate concordance across multiomic analyses and cancer types.

This concordance provides orthogonal support for our conclusions and indicates that single-cell heterogeneity and spatial organization of tumors may share similarities across different types of cancer and across different molecular assays. Our spatial analyses demonstrate the use of various algorithms to quantify the spatial landscape of tumors using single-cell imaging data. Further, our computational methods provide a framework for future single-cell imaging analyses, as they are applicable to any multiplex imaging assay, including mIHC, co-detection by indexing technology (CODEX) (7), cyclic immunofluorescence (18), and imaging mass cytometry (6). Our results highlight several spatial architectures that may help guide precision medicine approaches for HPV(-) HNSCC patients, including architectures that may help predict which patients will have shorter survival and thus warrant more aggressive therapy and clinical follow-up versus those that predict which patients have an improved survival outlook, where therapy and follow-up could be modulated. While our results provide evidence that the spatial organization of HPV(-) HNSCC tumors plays a role in clinical outcome, future studies on larger cohorts are needed to assess the full prognostic capabilities of the spatial features identified in our analyses.

ACKNOWLEDGEMENTS

The authors thank Dr. Courtney Betts, Justin Tibbitts, Teresa Beechwood, and Meghan Lavoie for regulatory and technical assistance. The authors thank the OHSU Knight

472 Biostatistics Shared Resource for guidance with statistical calculations. The authors
473 also acknowledge and thank the patients who donated tissue samples for this study.

REFERENCES

1. Binnewies M, Roberts EW, Kersten K, Chan V, Fearon DF, Merad M*, et al.* Understanding the tumor immune microenvironment (TIME) for effective therapy. Nat Med **2018**;24(5):541-50.
2. Junttila MR, de Sauvage FJ. Influence of tumour micro-environment heterogeneity on therapeutic response. Nature **2013**;501(7467):346-54.
3. Petitprez F, de Reynies A, Keung EZ, Chen TW, Sun CM, Calderaro J*, et al.* B cells are associated with survival and immunotherapy response in sarcoma. Nature **2020**;577(7791):556-60.
4. Keren L, Bosse M, Marquez D, Angoshtari R, Jain S, Varma S*, et al.* A Structured Tumor-Immune Microenvironment in Triple Negative Breast Cancer Revealed by Multiplexed Ion Beam Imaging. Cell **2018**;174(6):1373-87 e19.
5. Ali HR, Jackson HW, Zanotelli VRT, Danenberg E, Fischer JR, Bardwell H*, et al.* Imaging mass cytometry and multiplatform genomics define the phenogenomic landscape of breast cancer. Nature Cancer **2020**;1(2):163-75.
6. Jackson HW, Fischer JR, Zanotelli VRT, Ali HR, Mechera R, Soysal SD*, et al.* The single-cell pathology landscape of breast cancer. Nature **2020**;578(7796):615-20.
7. Schurch CM, Bhate SS, Barlow GL, Phillips DJ, Noti L, Zlobec I*, et al.* Coordinated Cellular Neighborhoods Orchestrate Antitumoral Immunity at the Colorectal Cancer Invasive Front. Cell **2020**.
8. Farkkila A, Gulhan DC, Casado J, Jacobson CA, Nguyen H, Kochupurakkal B*, et al.* Immunogenomic profiling determines responses to combined PARP and PD-1 inhibition in ovarian cancer. Nat Commun **2020**;11(1):1459.
9. Barua S, Fang P, Sharma A, Fujimoto J, Wistuba I, Rao AUK*, et al.* Spatial interaction of tumor cells and regulatory T cells correlates with survival in non-small cell lung cancer. Lung Cancer **2018**;117:73-9.
10. Gide TN, Silva IP, Quek C, Ahmed T, Menzies AM, Carlino MS*, et al.* Close proximity of immune and tumor cells underlies response to anti-PD-1 based therapies in metastatic melanoma patients. Oncoimmunology **2020**;9(1):1659093.
11. Giraldo NA, Nguyen P, Engle EL, Kaunitz GJ, Cottrell TR, Berry S*, et al.* Multidimensional, quantitative assessment of PD-1/PD-L1 expression in patients with Merkel cell carcinoma and association with response to pembrolizumab. J Immunother Cancer **2018**;6(1):99.
12. Johnson DB, Bordeaux J, Kim JY, Vaupel C, Rimm DL, Ho TH*, et al.* Quantitative Spatial Profiling of PD-1/PD-L1 Interaction and HLA-DR/IDO-1 Predicts Improved Outcomes of Anti-PD-1 Therapies in Metastatic Melanoma. Clin Cancer Res **2018**;24(21):5250-60.
13. Enfield KSS, Martin SD, Marshall EA, Kung SHY, Gallagher P, Milne K*, et al.* Hyperspectral cell sociology reveals spatial tumor-immune cell interactions associated with lung cancer recurrence. J Immunother Cancer **2019**;7(1):13.
14. Galon J, Costes A, Sanchez-Cabo F, Kirilovsky A, Mlecnik B, Lagorce-Pages C*, et al.* Type, density, and location of immune cells within human colorectal tumors predict clinical outcome. Science **2006**;313(5795):1960-4.

15. Galon J, Pages F, Marincola FM, Angell HK, Thurin M, Lugli A*, et al.* Cancer classification using the Immunoscore: a worldwide task force. J Transl Med **2012**;10:205.
16. Tsujikawa T, Kumar S, Borkar RN, Azimi V, Thibault G, Chang YH*, et al.* Quantitative Multiplex Immunohistochemistry Reveals Myeloid-Inflamed Tumor-Immune Complexity Associated with Poor Prognosis. Cell Rep **2017**;19(1):203-17.
17. Banik G, Betts CB, Liudahl SM, Sivagnanam S, Kawashima R, Cotechini T*, et al.* High-dimensional multiplexed immunohistochemical characterization of immune contexture in human cancers. Methods Enzymol **2020**;635:1-20.
18. Eng J, Thibault G, Luoh SW, Gray JW, Chang YH, Chin K. Cyclic Multiplexed-Immunofluorescence (cmIF), a Highly Multiplexed Method for Single-Cell Analysis. Methods Mol Biol **2020**;2055:521-62.
19. Brucher BL, Jamall IS. Cell-cell communication in the tumor microenvironment, carcinogenesis, and anticancer treatment. Cell Physiol Biochem **2014**;34(2):213-43.
20. Alsahafi E, Begg K, Amelio I, Raulf N, Lucarelli P, Sauter T*, et al.* Clinical update on head and neck cancer: molecular biology and ongoing challenges. Cell Death Dis **2019**;10(8):540.
21. Cohen EEW, Bell RB, Bifulco CB, Burtness B, Gillison ML, Harrington KJ*, et al.* The Society for Immunotherapy of Cancer consensus statement on immunotherapy for the treatment of squamous cell carcinoma of the head and neck (HNSCC). J Immunother Cancer **2019**;7(1):184.
22. Canning M, Guo G, Yu M, Myint C, Groves MW, Byrd JK*, et al.* Heterogeneity of the Head and Neck Squamous Cell Carcinoma Immune Landscape and Its Impact on Immunotherapy. Front Cell Dev Biol **2019**;7:52.
23. Fakhry C, Westra WH, Li S, Cmelak A, Ridge JA, Pinto H*, et al.* Improved survival of patients with human papillomavirus-positive head and neck squamous cell carcinoma in a prospective clinical trial. J Natl Cancer Inst **2008**;100(4):261-9.
24. Ang KK, Harris J, Wheeler R, Weber R, Rosenthal DI, Nguyen-Tan PF*, et al.* Human papillomavirus and survival of patients with oropharyngeal cancer. N Engl J Med **2010**;363(1):24-35.
25. Virtanen P, Gommers R, Oliphant TE, Haberland M, Reddy T, Cournapeau D*, et al.* SciPy 1.0: fundamental algorithms for scientific computing in Python. Nat Methods **2020**;17(3):261-72.
26. Pedregosa F, Varoquaux G, Gramfort A, Michel V, Thirion B, Grisel O*, et al.* Scikit-learn: Machine Learning in Python. JMLR **2011**;12:2825-30.
27. Davidson-Pilon C, Kalderstam J, Jacobson N, sean-reed, Kuhn B, Zivich P*, et al.* CamDavidsonPilon/lifelines: v0.21.0. Zenodo **2020**.
28. Predina J, Eruslanov E, Judy B, Kapoor V, Cheng G, Wang LC*, et al.* Changes in the local tumor microenvironment in recurrent cancers may explain the failure of vaccines after surgery. Proc Natl Acad Sci U S A **2013**;110(5):E415-24.
29. Zheng B, Wang J, Cai W, Lao I, Shi Y, Luo X*, et al.* Changes in the tumor immune microenvironment in resected recurrent soft tissue sarcomas. Ann Transl Med **2019**;7(16):387.

30. Walens A, Lin J, Damrauer JS, McKinney B, Lupo R, Newcomb R*, et al.* Adaptation and selection shape clonal evolution of tumors during residual disease and recurrence. Nat Commun **2020**;11(1):5017.
31. Hartman DJ, Ahmad F, Ferris RL, Rimm DL, Pantanowitz L. Utility of CD8 score by automated quantitative image analysis in head and neck squamous cell carcinoma. Oral Oncol **2018**;86:278-87.
32. Balermpas P, Rodel F, Rodel C, Krause M, Linge A, Lohaus F*, et al.* CD8+ tumour-infiltrating lymphocytes in relation to HPV status and clinical outcome in patients with head and neck cancer after postoperative chemoradiotherapy: A multicentre study of the German cancer consortium radiation oncology group (DKTK-ROG). Int J Cancer **2016**;138(1):171-81.
33. Nasman A, Romanitan M, Nordfors C, Grun N, Johansson H, Hammarstedt L*, et al.* Tumor infiltrating CD8+ and Foxp3+ lymphocytes correlate to clinical outcome and human papillomavirus (HPV) status in tonsillar cancer. PLoS One **2012**;7(6):e38711.
34. Nordfors C, Grun N, Tertipis N, Ahrlund-Richter A, Haeggblom L, Sivars L*, et al.* CD8+ and CD4+ tumour infiltrating lymphocytes in relation to human papillomavirus status and clinical outcome in tonsillar and base of tongue squamous cell carcinoma. Eur J Cancer **2013**;49(11):2522-30.
35. Marcus B, Arenberg D, Lee J, Kleer C, Chepeha DB, Schmalbach CE*, et al.* Prognostic factors in oral cavity and oropharyngeal squamous cell carcinoma. Cancer **2004**;101(12):2779-87.
36. Wolf GT, Chepeha DB, Bellile E, Nguyen A, Thomas D, McHugh J*, et al.* Tumor infiltrating lymphocytes (TIL) and prognosis in oral cavity squamous carcinoma: a preliminary study. Oral Oncol **2015**;51(1):90-5.
37. Fridman WH, Pages F, Sautes-Fridman C, Galon J. The immune contexture in human tumours: impact on clinical outcome. Nat Rev Cancer **2012**;12(4):298-306.
38. Freeman GJ, Long AJ, Iwai Y, Bourque K, Chernova T, Nishimura H*, et al.* Engagement of the PD-1 immunoinhibitory receptor by a novel B7 family member leads to negative regulation of lymphocyte activation. J Exp Med **2000**;192(7):1027-34.
39. Akinleye A, Rasool Z. Immune checkpoint inhibitors of PD-L1 as cancer therapeutics. J Hematol Oncol **2019**;12(1):92.
40. Kleffel S, Posch C, Barthel SR, Mueller H, Schlapbach C, Guenova E*, et al.* Melanoma Cell-Intrinsic PD-1 Receptor Functions Promote Tumor Growth. Cell **2015**;162(6):1242-56.
41. Du S, McCall N, Park K, Guan Q, Fontina P, Ertel A*, et al.* Blockade of Tumor-Expressed PD-1 promotes lung cancer growth. Oncoimmunology **2018**;7(4):e1408747.
42. Li H, Li X, Liu S, Guo L, Zhang B, Zhang J*, et al.* Programmed cell death-1 (PD-1) checkpoint blockade in combination with a mammalian target of rapamycin inhibitor restrains hepatocellular carcinoma growth induced by hepatoma cell-intrinsic PD-1. Hepatology **2017**;66(6):1920-33.
43. Parajuli H, Teh MT, Abrahamsen S, Christoffersen I, Neppelberg E, Lybak S*, et al.* Integrin alpha11 is overexpressed by tumour stroma of head and neck

612 squamous cell carcinoma and correlates positively with alpha smooth muscle
613 actin expression. J Oral Pathol Med **2017**;46(4):267-75.
614 44. Shiga K, Hara M, Nagasaki T, Sato T, Takahashi H, Takeyama H. Cancer-
615 Associated Fibroblasts: Their Characteristics and Their Roles in Tumor Growth.
616 Cancers (Basel) **2015**;7(4):2443-58.
617 45. Tao L, Huang G, Song H, Chen Y, Chen L. Cancer associated fibroblasts: An
618 essential role in the tumor microenvironment. Oncol Lett **2017**;14(3):2611-20.
619 46. Sahai E, Astsaturov I, Cukierman E, DeNardo DG, Egeblad M, Evans RM*, et al.*
620 A framework for advancing our understanding of cancer-associated fibroblasts.
621 Nat Rev Cancer **2020**;20(3):174-86.
622 47. Johansson AC, Ansell A, Jerhammar F, Lindh MB, Grenman R, Munck-Wikland
623 E*, et al.* Cancer-associated fibroblasts induce matrix metalloproteinase-mediated
624 cetuximab resistance in head and neck squamous cell carcinoma cells. Mol
625 Cancer Res **2012**;10(9):1158-68.
626 48. Wood O, Clarke J, Woo J, Mirza AH, Woelk CH, Thomas GJ*, et al.* Head and
627 Neck Squamous Cell Carcinomas Are Characterized by a Stable Immune
628 Signature Within the Primary Tumor Over Time and Space. Clin Cancer Res
629 **2017**;23(24):7641-9.
630 49. Reuben A, Spencer CN, Prieto PA, Gopalakrishnan V, Reddy SM, Miller JP*, et*
631 *al.* Genomic and immune heterogeneity are associated with differential
632 responses to therapy in melanoma. NPJ Genom Med **2017**;2.
633 50. Zhang Q, Lou Y, Yang J, Wang J, Feng J, Zhao Y*, et al.* Integrated multiomic
634 analysis reveals comprehensive tumour heterogeneity and novel
635 immunophenotypic classification in hepatocellular carcinomas. Gut
636 **2019**;68(11):2019-31.
637 51. Lin W, Noel P, Borazanci EH, Lee J, Amini A, Han IW*, et al.* Single-cell
638 transcriptome analysis of tumor and stromal compartments of pancreatic ductal
639 adenocarcinoma primary tumors and metastatic lesions. Genome Med
640 **2020**;12(1):80.
641 52. Gyanchandani R, Lin Y, Lin HM, Cooper K, Normolle DP, Brufsky A*, et al.*
642 Intratumor Heterogeneity Affects Gene Expression Profile Test Prognostic Risk
643 Stratification in Early Breast Cancer. Clin Cancer Res **2016**;22(21):5362-9.

Blise et al. Table 1

Cell Phenotype	Antibody Markers
$CD8^+$ T Cell	$CD45^+$ $CD20^-$ $CD3^+$ $CD8^+$
$CD4^+$ T Helper	$CD45^+$ $CD20^-$ $CD3^+$ $CD8^-$ $FOXP3^-$
$CD4^+$ Regulatory T Cell	$CD45^+$ $CD20^-$ $CD3^+$ $CD8^-$ $FOXP3^+$
B Cell	$CD45^+$ $CD20^+$
Macrophage	$CD45^+$ $CD20^-$ $CD3^-$ $CD66B^-$ $CD68^+$
Granulocyte	$CD45^+$ $CD20^-$ $CD3^-$ $CD66B^+$
Dendritic Cell	$CD45^+$ $CD20^-$ $CD3^-$ $CD66B^-$ $CD68^-$ $MHCII^+$
Other Immune	$CD45^+$ $CD20^-$ $CD3^-$ $CD66B^-$ $CD68^-$ $MHCII^-$
αSMA^+ Mesenchymal	$CD45^-$ $PANCK^-$ αSMA^+
Other Non-Immune	$CD45^-$ $PANCK^-$ αSMA^-
Neoplastic Tumor	$CD45^-$ $PANCK^+$
Additional Functional Markers: PD-1, PD-L1, Ki-67	

Table 1. mIHC cell phenotype classification. Antibody markers used to hierarchically phenotype cells into one of eleven phenotype classifications. Additional functional markers stained are listed at the bottom.

Characteristic	n (%)
Gender	Female: 7 (78%) Male: 2 (22%)
Race	Asian: 1 (11%) White: 8 (89%)
Average Age at Primary Surgery	61 years
Alcohol History	Yes: 7 (78%) No: 2 (22%)
Smoking History	Yes: 5 (56%) No: 4 (44%)
HPV Status	Positive: 0 (0%) Negative: 9 (100%)
Tumor Site	Larynx: 3 (33%) Oral Cavity: 4 (44%) Oropharynx: 2 (22%)
TNM Stage	Stage 1: 2 (22%) Stage 2: 1 (11%) Stage 3: 1 (11%) Stage 4: 5 (56%)
Therapy Following Primary Resection	Cisplatin + Radiation: 6 (67%) Cetuximab + Radiation: 3 (33%)
Average Progression Free Survival	504 days (1.4 years)

Table 2. Patient and tumor characteristics. Adapted from Banik et al (17).

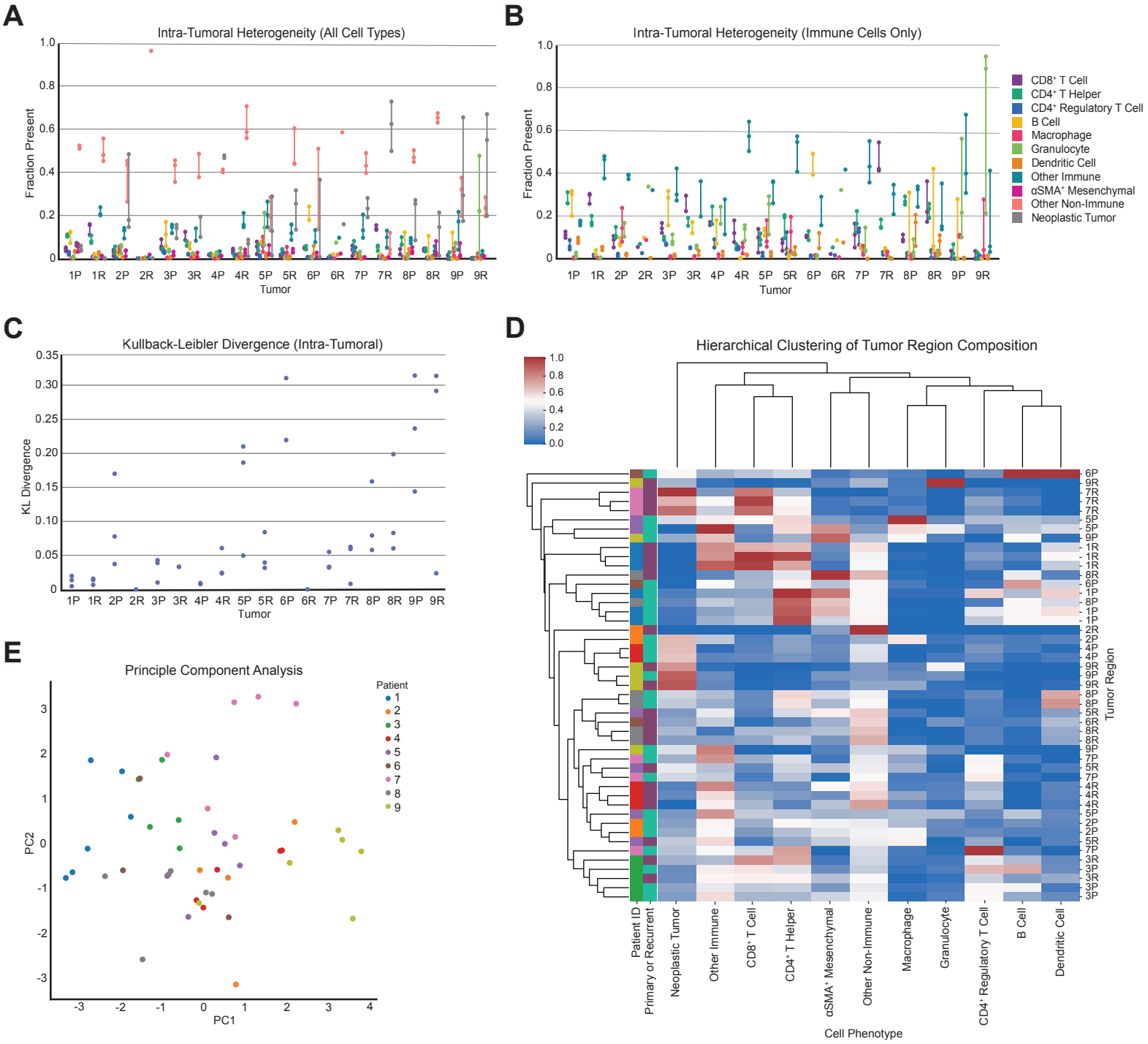

Figure 1. Heterogeneity across patients and tumor regions. A, Fraction (out of 1.0) of each cell type present per individual primary (P) and recurrent (R) tumor. Each dot represents a single tumor region (n=47). **B**, Fraction (out of 1.0) of each immune cell type present per individual primary (P) and recurrent (R) tumor. Each dot represents a single tumor region (n=47). **C**, Dot plot of the Kullback-Leibler divergence from a single tumor region's cellular distribution compared to the tumor's average cellular distribution. **D**, Heatmap of cellular composition across tumor regions. Rows are individual tumor regions that are ordered by the hierarchical clustering of their cellular composition. Columns are the cell types used as clustering features. Composition was normalized [0,1] before clustering. Leftmost column is color coded by patient. Next column is color coded by tumor type. **E**, Principal component analysis on cellular composition. Each dot (n=47) represents one tumor region and is colored by patient.

Blise et al. Figure 2

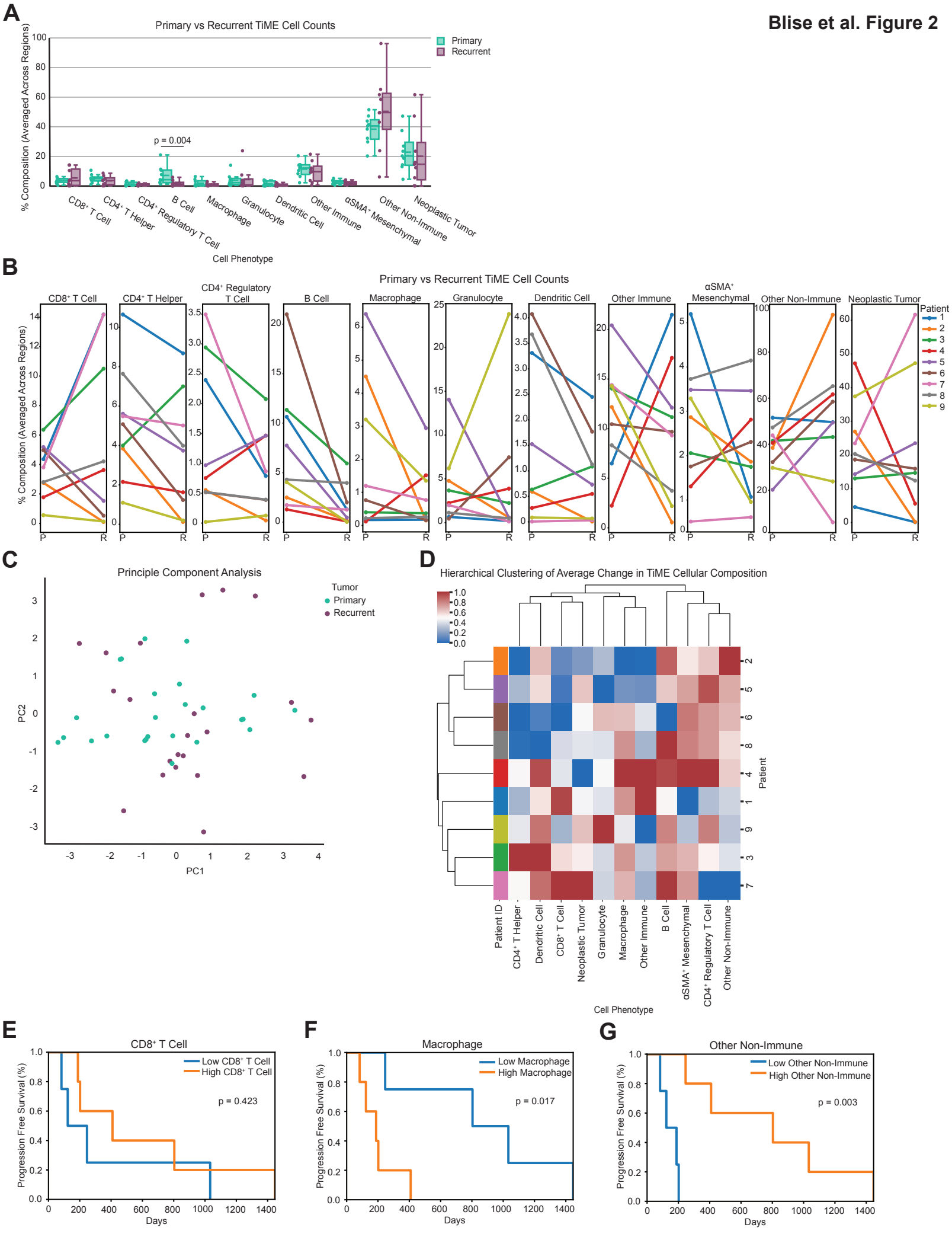

Figure 2. Tumor cellular composition changes following therapy and composition associations with survival. A, Box plot showing the percent that each cell type contributes to each tumor's cellular makeup. Each dot represents the percent contribution of that cell type for one tumor, averaged across regions (n=9 primary tumors, n=9 recurrent tumors). Statistical significance calculated using parametric paired two-tailed t-tests for cell types whose differences follow a normal distribution and non-parametric paired two-tailed t-tests (Wilcoxon signed rank test) for cell types whose differences do not follow a normal distribution. **B**, Line plots showing the change in cellular composition from primary to recurrent tumors for each cell type. Each dot represents the percent contribution of that cell type for one tumor, averaged across regions. Lines are colored by patient. **C**, Principal component analysis on cellular composition. Each dot (n=47) represents one tumor region and is colored by its primary or recurrent designation. **D**, Heatmap of average change in cellular composition from primary to recurrent tumors for each patient. Rows are individual patients that are ordered by the hierarchical clustering of their change in TiME cellular composition (averaged across regions). Columns are the cell types used as clustering features. Compositional change was normalized [0,1] before clustering. Leftmost column is color coded by patient. **E**, Kaplan-Meier curve of progression free survival for patients split by the percentage of $CD8^+$ T cells in their primary tumors. Patients were split on the median value. P-value calculated using the log-rank test. **F**, Kaplan-Meier curve of progression free survival for patients split by the percentage of macrophages in their primary tumors. Patients were split on the median value. P-value calculated using the log-rank test. **G**, Kaplan-Meier curve of progression free survival for patients split by the percentage of other non-immune, non-neoplastic cells in their primary tumors. Patients were split on the median value. P-value calculated using the log-rank test.

Blise et al. Figure 3

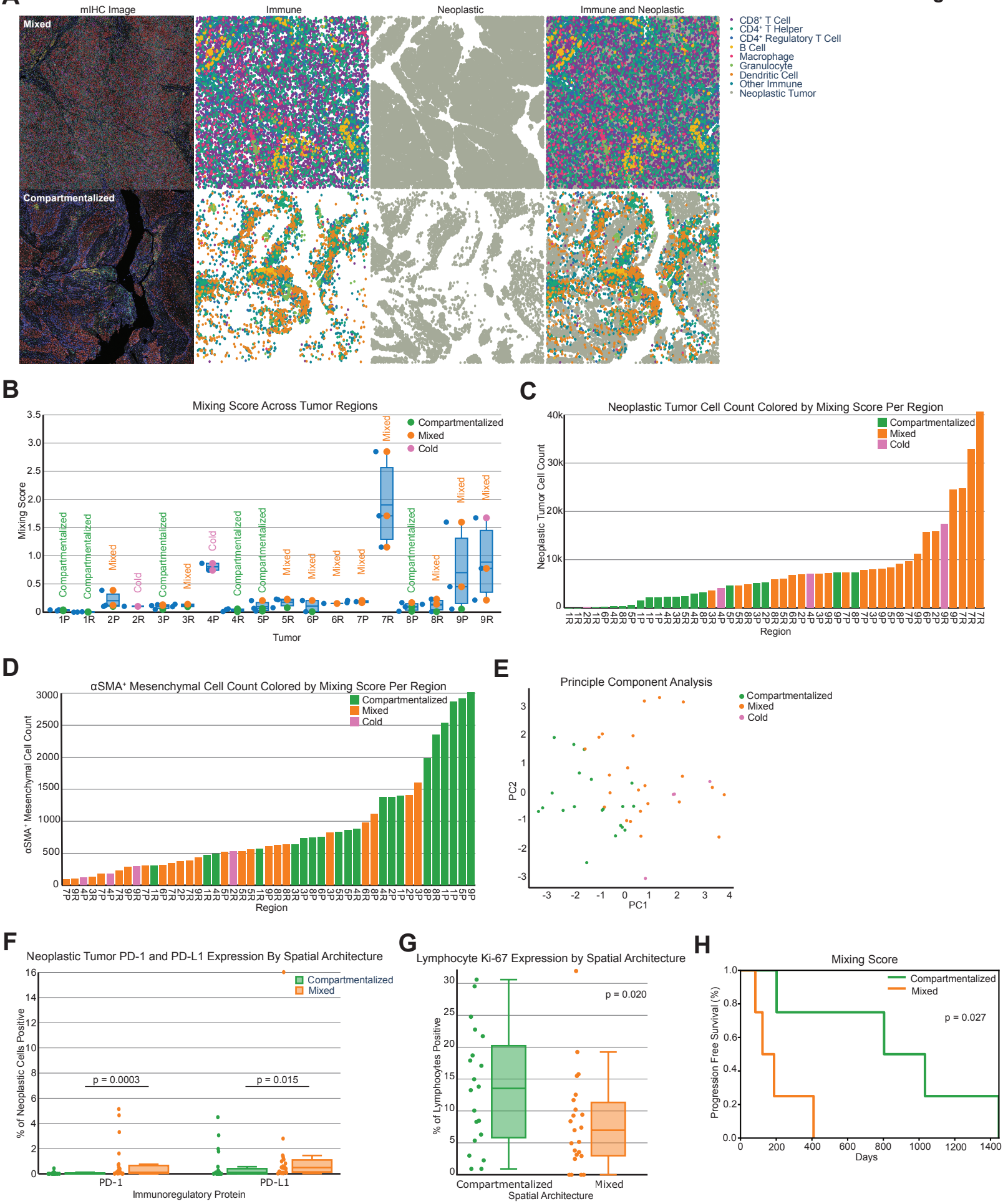

Figure 3. Mixing score quantifies the spatial organization of tumors. A, Mixed tumor region (top) versus compartmentalized tumor region (bottom). Leftmost panel is the mIHC image of the tumor region (red = neoplastic tumor; blue = non-neoplastic, non-immune; other colors = immune). Remaining panels show scatterplot reconstructions of the mIHC image, excluding the non-immune, non-neoplastic cells. Each dot represents one cell, and is colored by cell type. **B**, Box plot showing the mixing scores across all primary and recurrent tumors (n=18). Each dot (n=47) represents the mixing score for one tumor region and is colored according to its spatial architecture. The average spatial architecture designation for the overall tumor is printed above each box. **C**, Bar chart showing the raw count of neoplastic tumor cells present per tumor region. Bars are ordered by neoplastic cell count and are colored according to the region's spatial architecture. **D**, Bar chart showing the raw count of αSMA^+ mesenchymal cells present per tumor region. Bars are ordered by αSMA^+ cell count and are colored according to the region's spatial architecture. **E**, Principal component analysis on cellular composition. Each dot (n=47) represents one tumor region and is colored according to the region's spatial architecture. **F**, PD-1 and PD-L1 expression on neoplastic tumor cells by spatial architecture. Each dot represents the percentage of neoplastic cells positive for that immunoregulatory protein for a single tumor region (n=43, excluding cold regions). P-values calculated using a one-tailed Mann-Whitney U test. **G**, Ki-67 expression on lymphocytes ($CD8^+$ T cells, $CD4^+$ Regulatory T cells, $CD4^+$ T Helper, and B cells) by spatial architecture. Each dot represents the percentage of lymphocytes positive for Ki-67 for a single tumor region (n=43, excluding cold regions). P-value calculated using a one-tailed t-test. **H**, Kaplan-Meier curve of progression free survival for patients split by the mixing score of their primary tumors. Patients were split on the median value. Results exclude cold tumor regions. P-value calculated using the log-rank test.

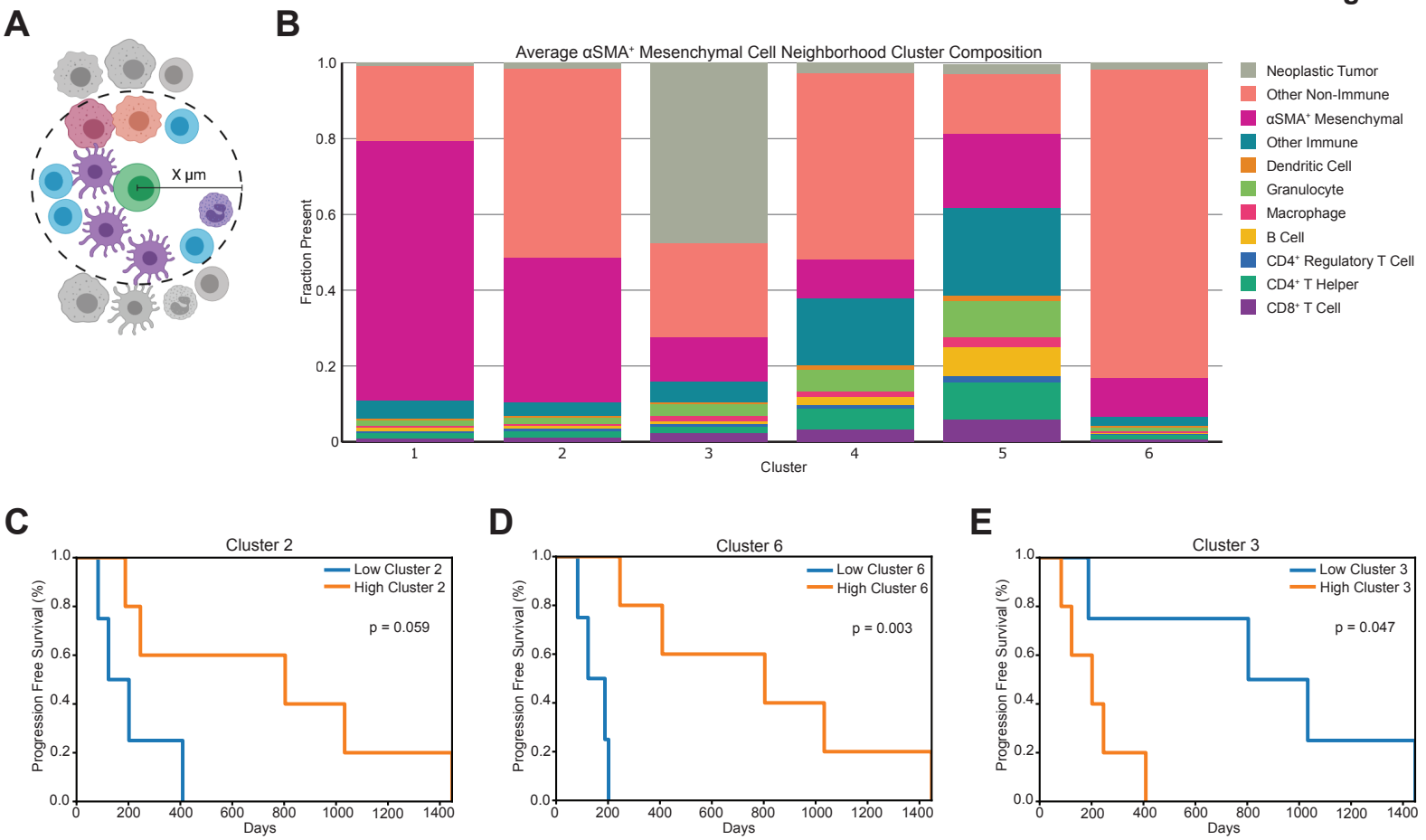

Figure 4. αSMA⁺ mesenchymal cellular neighborhood clustering. **A**, Cellular neighborhoods were defined by drawing a circle of a specified radius around each seed cell (green) of a designated phenotype. Cells whose centers were inside the circle were considered neighbors of that seed cell. This figure was created using BioRender.com. **B**, Stacked bar chart showing the average cellular composition of each αSMA⁺ mesenchymal cell neighborhood cluster (n=6). Bars are colored by cell type and represent the average fraction (out of 1.0) of each cell type present in the neighborhoods belonging to each cluster. **C**, Kaplan-Meier curve of progression free survival for patients split by the percentage of αSMA⁺ mesenchymal cell neighborhoods belonging to cluster 2 in their primary tumors. Patients were split on the median value. P-value calculated using the log-rank test. **D**, Kaplan-Meier curve of progression free survival for patients split by the percentage of αSMA⁺ mesenchymal cell neighborhoods belonging to cluster 6 in their primary tumors. Patients were split on the median value. P-value calculated using the log-rank test. **E**, Kaplan-Meier curve of progression free survival for patients split by the percentage of αSMA⁺ mesenchymal cell neighborhoods belonging to cluster 3 in their primary tumors. Patients were split on the median value. P-value calculated using the log-rank test.